Experimental Evidence of Velocity-Weakening Friction during Ice Slip over Frozen Till: Implications for Basal Seismicity in Fast Moving, Soft-Bed Glaciers and Ice Streams

Seth Saltiel*[1], Christine McCarthy[1], Timothy T. Creyts[1], and Heather M. Savage[2]

Abstract

Observations of glacier slip over till beds, across a range of spatial and temporal scales, show abundant seismicity ranging from $M_w \sim -2$ microearthquakes and tremor (submeter asperities and millisecond duration) to $M_w \sim 7$ slow-slip events (~ 50 km rupture lengths and ~ 30 min durations). A complete understanding of the mechanisms capable of producing seismic signals in these environments represents a strong constraint on bed conditions. In particular, there is a lack of experimental confirmation of velocity-weakening behavior of ice slipping on till, where friction decreases with increasing velocity—a necessity for nucleating seismic slip. To measure the frictional strength and stability of ice sliding against till, we performed a series of double-direct-shear experiments at controlled temperatures slightly above and below the ice melting point. Our results confirm velocity-strengthening ice–till slip at melting temperatures, as has been found in the few previous studies. We provide best-fit rate-and-state friction parameters and their standard deviations from averaging 13 experiments at equivalent conditions. We find evidence of similar velocity-strengthening behavior with 50% by volume debris-laden ice slid against till under the same conditions. In contrast, velocity-weakening and linear time-dependent healing of ice–till slip is present at temperatures slightly below the melting point, providing an experimentally supported mechanism for subglacial seismicity on soft-beds. The stability parameter (a–b) decreases with slip velocity, and evolution occurs over large (mm scale) displacements, suggesting that shear heating and melt buildup is responsible for the weakening. These measurements provide insight into subglacial stiffness in which seismicity of this type might be expected. We discuss glaciological circumstances pointing to potential field targets in which to test this frozen seismic asperity hypothesis.

Cite this article as Saltiel, S., C. McCarthy, T. T. Creyts, and H. M. Savage (2021). Experimental Evidence of Velocity-Weakening Friction during Ice Slip over Frozen Till: Implications for Basal Seismicity in Fast Moving, Soft-Bed Glaciers and Ice Streams, *Seismol. Res. Lett.* **XX**, 1–18, doi: 10.1785/0220200480.

Supplemental Material

Introduction

The mass balance and stability of the Greenland and Antarctic Ice Sheets are largely controlled by the dynamics of fast-moving outlets to the ocean, including outlet glaciers and ice streams (Bennett, 2003). Ice streams are fast-flowing rivers of ice embedded in a background of slower moving ice. Even though stresses driving flow are low, they slip quickly due to high water pressure and lubrication from till, unlithified sediment that deforms under shear (Cuffey and Paterson, 2010). Basal shear stresses are not uniform. Driving stresses are distributed among regions of very high basal stress, but areas between experience very low basal shear with almost freely slipping ice (Joughin, MacAyeal, and Tulacyzk, 2004; Sergienko *et al.*, 2014). Areas of high ice-bed coupling are analogous to fault asperities, but they are not necessarily correlated with seismic slip. An exception is, particularly, well-studied Whillans Ice Stream (WIS) and a large asperity on its ice plain, which fails in tidally triggered slow-slip events

---

1. Lamont-Doherty Earth Observatory, The Earth Institute, Columbia University of New York, New York, U.S.A., https://orcid.org/0000-0002-8058-6894 (SS); https://orcid.org/0000-0002-5276-5246 (CM); https://orcid.org/0000-0003-1756-5211 (TTC); 2. Department of Earth and Planetary Sciences, University of California, Santa Cruz, California, U.S.A., https://orcid.org/0000-0002-5773-7279 (HMS)

*Corresponding author: saltiel@ldeo.columbia.edu

(accompanied by tremor and basal icequakes), accounting for most of the total surface velocity in this location (Winberry *et al.*, 2013). WIS is also one of the few slowing glacial features, and observations suggest that increasing basal resistance and stick-slip are the main cause of deceleration (Joughin *et al.*, 2005; Beem *et al.*, 2014; Winberry *et al.*, 2014). Basal seismicity has been observed in a range of glacial settings responding to tidal stresses (Zoet *et al.*, 2012), meltwater (Roeoesli *et al.*, 2016), contrasts in till properties (Smith, 2006), occurring in both active and shutdown ice streams (Anandakrishnan and Bentley, 1993), topographic lows of mega-scale glacial lineations (Barcheck *et al.*, 2020), and as stable, migrating, or short-lived tremor (Kufner *et al.*, 2020; McBrearty *et al.*, 2020), all suggesting the ubiquity of unstable basal sliding (Umalauft *et al.*, 2020). Bed conditions are largely inaccessible, but seismicity provides the potential to remotely monitor basal evolution with a sufficient understanding of seismic slip mechanics.

Bed strength is determined by the conditions there to first order whether ice overlies hard bedrock or soft till (Clarke, 2005). Although, ice streams are assumed to be largely overlying till, very few ice-on-till friction experiments have been published, none showing stick-slip. Experiments on fault materials have shown that ability to nucleate earthquakes is determined by frictional properties and elastic stiffness of the loading medium (Leeman *et al.*, 2016), in agreement with stability theory (Gu *et al.*, 1984). Specifically, stick-slip motion requires that bed deformation exhibits two behaviors: (1) rate weakening or friction decreasing with increases in slip velocity, allowing acceleration during slip events; and (2) healing, allowing elastic stress to build up during stick intervals. Both have been experimentally observed in fault rocks and gouge (Marone, 1998). Diverse granular deformation tests (triaxial, double-direct shear, and ring shear) of till samples exhibit essentially rate-neutral behavior, suggesting that till deformation itself is not generally responsible for seismicity, but some tills could satisfy this criterion (Iverson, 2010). Ice–till sliding experiments have shown sufficient healing with holds on tidal time scales (Zoet and Iverson, 2018), but rate weakening has remained elusive. Zoet and Iverson (2020) found velocity-strengthening in ice–till slip at the pressure melting point, explained by a model where shear stress grows at low velocities, dominated by viscous ice flow around till grain protrusions or clasts, until shear stress in the ice reaches the rate-independent strength of till at higher velocities. Those measurements were made with a high permeability till to ensure complete drainage. Pore-pressure feedbacks have been shown to produce velocity weakening from clast plowing in low diffusivity till, whereby compression in front of clasts causes lower effective stress (Thomason and Iverson, 2008). This mechanism is limited to velocities high enough to build up pore pressure before it defuses away, whereas, porosity will reach a minimum at a certain compaction speed. As plowing experiments were done without ice, confirmation is needed that till is softer than ice during the velocity range where the pore-pressure feedback is active, so velocity weakening is expressed. Lipovsky *et al.* (2019) measured rate-strengthening behavior for pure ice-on-till slip at the pressure melting point up to 30 μm/s (~950 m/yr), concluding that the higher effective stresses needed for unstable slip would ensure sediment entrainment, thus debris-laden ice might contribute to velocity-weakening behavior. This idea aligns with experiments of debris-laden ice on rock showing velocity weakening at velocities above 16μm/s (~500 m/yr) at −3°C (Zoet *et al.*, 2013). These same conditions also exhibited stick-slip cycles and stress drops, when the apparatus stiffness was lowered (Zoet *et al.*, 2020). Pure ice-on-rock friction has also been found to be velocity weakening at temperatures below −18° C (McCarthy *et al.*, 2017), suggesting subfreezing temperatures could contribute to seismic behaviors on till beds as well. Basal freezing and melting have been proposed to regulate the evolution of strength in soft beds, during both stick and slip phases (Tulaczyk *et al.*, 2000; Christoffersen and Tulaczyk, 2003; Winberry *et al.*, 2009). We test the effect of temperate and frozen conditions, but other hypotheses for ice–till seismicity, such as drained, low-porosity till (Anandakrishnan and Bentley, 1993) and overconsolidated (lodgment) till (Barcheck *et al.*, 2018), have not been shown experimentally.

The combination of ubiquitous seismic observations across scales and subglacial settings with a lack of experimentally verified mechanisms for obtaining this behavior presents an opportunity for improving constraints on bed processes and conditions. We conducted a series of experiments testing different potential scenarios of deformation at the base of ice streams, including wet till-only, temperate pure ice-on-till, temperate debris-laden ice-on-till, pure ice-on-frozen till, and debris-laden ice-on-frozen till. We present the first experimental evidence of velocity weakening in an ice–till slip setting that of pure ice-on-frozen till at temperatures slightly below the pressure melting point. We then discuss the relevant conditions and constraints of this ice sheet basal seismicity mechanism, representing a testable hypothesis for future field exploration.

Background

Rate-and-state friction formulation and stability theory

Stick-slip instability is commonly described in faults using the empirically derived rate-and-state friction formulation, which is dependent on slip-rate (or velocity) and one (or more) internal-state variables (Dieterich, 1979; Ruina, 1983)

$$\mu(v(t), \theta(t)) = \mu_0 + a \ln\left(\frac{v(t)}{v_0}\right) + b \ln\left(\frac{v_0 \theta(t)}{D_c}\right), \qquad (1)$$

in which μ is the current friction coefficient (shear stress τ divided by effective normal stress σ, overburden minus pore pressure); v is the current slip velocity, which can change with time; μ_0 is the reference friction coefficient (steady-state friction when $v = v_0$); v_0 is a characteristic velocity, often chosen as the lowest experimental velocity or long-term geological displacement rate; D_c is the critical slip distance, the distance over which state evolves to a new steady-state; θ is the state variable, commonly interpreted as representing the age of contacts, with units of time, related to porosity or dilation in granular layers (Segall and Rice, 1995); a is the parameter that determines the amplitude of the "direct effect," the friction change immediately following changes in velocity; and b determines the amount friction changes due to state evolution.

There are two primarily used laws for describing state evolution—the aging (Dietrich) law, which evolves in time even without slip (Dieterich, 1979)

$$\frac{d\theta}{dt} = 1 - \frac{v\theta}{D_c}, \tag{2}$$

and the slip (Ruina) law, which requires slip for state evolution (Ruina, 1983):

$$\frac{d\theta}{dt} = -\frac{v\theta}{D_c}\ln\left(\frac{v\theta}{D_c}\right). \tag{3}$$

The aging law is the simpler and more often used evolution law, although, recent studies show that the slip law is consistent with a wider range of data (Bhattacharya *et al.*, 2017). Other forms of rate-and-state friction have been developed to incorporate theory of subglacial cavity formation on hard beds (Thøgersen *et al.*, 2019), but we focus on conventional formulations in this study.

Steady state is reached over a slip distance D_c, when the state variable (θ) relaxes to its steady-state value and the evolution equation reaches zero. Equation (1) can then be rewritten as

$$\mu_{ss}(v_{ss}) = \mu_0 + (a - b)\ln\left(\frac{v_{ss}}{v_0}\right), \tag{4}$$

in which μ_{ss} is the steady-state friction value, and v_{ss} is the steady-state velocity. For a given set of a and b, their difference $(a - b)$ is called the stability parameter, and it determines the change in steady-state friction with a change in velocity. In this way, if friction increases with an increase in velocity ($a - b > 0$), it is called velocity strengthening, and, if friction decreases with an increase in velocity ($a - b < 0$), it is called velocity weakening.

Velocity-weakening friction is needed for rupture nucleation, because, as slip starts to accelerate, the feedback from decreasing friction promotes unstable acceleration. It is a necessary but an insufficient condition. Stick-slip generation is produced by a force imbalance between the elastic driving stress and resistance; friction must reduce faster than built up elastic energy is released. Thus, instability occurs when the stiffness of the surrounding medium (k), elastic stress change with displacement, is less than a rheological critical stiffness (k_{cr}), friction reduction with slip

$$k < k_{cr} = \left(\frac{-(a - b)\sigma}{D_c}\right), \tag{5}$$

in which σ is the effective normal stress, as defined earlier. Experiments often need to lower apparatus stiffness to capture stick-slip (Zoet *et al.*, 2020). Velocity weakening is required to achieve this condition ($k_{cr} < 0$ when $a - b > 0$), but, if rupture is already initiated, inertia or thermal weakening at high slip speeds can propagate seismic slip through velocity-strengthening regions. Strong elastic contrasts, such as between ice and rock, can cause nucleation at nominally slightly stable situations ($k_{cr} < k$) (Rice *et al.*, 2001), and slow-slip events have been shown as expressions of conditional stability ($k_{cr} \sim k$) (Leeman *et al.*, 2016), so this boundary is not a strict limit but a useful guide for when stick-slip is expected.

The chief advantages of rate-and-state friction is its ability to describe transient behaviors not at steady state, particularly, seismic stick-slip cycles, with a large literature of modeling and experimental studies for a wide range of geological materials and conditions (Scholz, 2002). Although, not yet widespread, experimental (McCarthy *et al.*, 2017; Zoet *et al.*, 2020) and numerical (Thøgersen *et al.*, 2019; Minchew and Meyer, 2020) studies have begun to argue for the use of rate-and-state friction in glacier settings with unsteady slip velocities.

Methods and Materials

Our experiments used a sample assembly that consists of a double-direct-shear configuration, with a central sliding ice block (or steel block for till-only deformation) and two stationary side blocks with layers of precompacted till on opposite sides of the ice (Fig. 1). In this section, we will describe each of these components (ice and till)—the sample assembly, the apparatus, and the experimental procedure.

Ice sample types

We created three different types of ice samples. First, a modified version of the "standard ice" method was employed (Cole, 1979), in which seed ice was sieved between 108 and 250 μm mesh sieves and then packed into a die layer by layer. The die was then equilibrated in a zero-degree bath and slowly flooded under vacuum until all the pore space filled with deionized water. The two-phase mixture was then frozen slowly from the bottom up to allow air bubbles to escape and minimize the final porosity. We also created bulk ice samples, frozen in the same way but with the die filled only with deionized water, resulting in large, nonuniform grain size. We find the difference in the frictional behavior between the two types of samples insignificant (see the Supplement Section S1) and, thus, present results from mostly bulk solidification samples, as they are much less time consuming to construct. These rectangular pure ice samples are intentionally frozen oversized and cut down to 50 × 50 × 100 mm, with a microtome housed in a cold room (~ -12°C). The sliding surfaces were then roughened with a number 100 grit sandpaper using the same procedure as described by McCarthy *et al.* (2017), who determined a roughness average (R_a) of 7 ± 1 μm using a profilometer (Mitutoyo SF-210).

Lastly, to test the hypothesis that debris-laden ice provides rock–till friction capable of velocity-weakening behavior and, thus, seismic stick-slip (Lipovsky *et al.*, 2019), we created a 50% by volume debris-laden ice sample, as this was found to be the debris content in which rock debris dominates the overall mechanics (Moore, 2014). In this case, we followed the method described previously, but used seed ice of between 250 μm and 1 mm in diameter. This seed ice was packed in the die with even volumes of Matanuska till grains between 1 and 4 mm in diameter (less than 1/10th the smallest dimension of the ice sample of 50 mm), mixing and compacting layer by layer. Larger till grains were selected, as they are theorized to be the first to be entrained in the ice at the lowest effective normal stresses (Meyer *et al.*, 2018). Also, the transition to debris-dominated "sandy" friction depends on rock grain size, as larger grains are more likely to bridge any melt film and protrude into the bed (Emerson and Rempel, 2007). The ice–debris mixture was then flooded and frozen, following the "standard ice" procedure outlined earlier. This die was not oversized, so no cutting or roughening was done to the final sample. The debris on the sample surface creates much higher roughness than that of the pure ice samples. The roughness of the samples as fabricated was outside of the profilometer range.

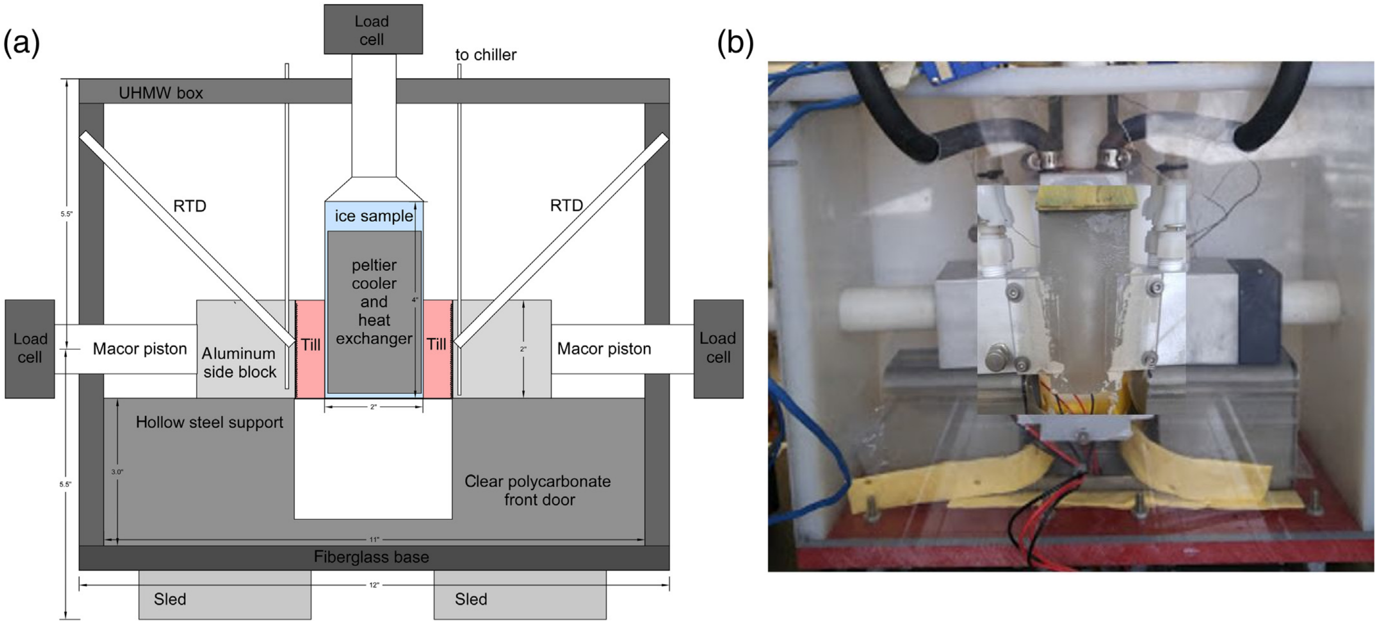

Figure 1. (a) Design and (b) photograph of biaxial cryostat designed for ice–till experiments. Photo has overset to show the ice sample below the front Peltier cooler and heat exchanger. RTD, resistance temperature detector; UHMW, ultra high molecular weight. The color version of this figure is available only in the electronic edition.

Till source and layer preparation

All experiments were undertaken using till from the Matanuska glacier—a large (~45 km long) valley glacier flowing north from the ice fields of the Chugach Mountains in south-central Alaska (Lawson *et al.*, 1998). Matanuska till has previously been studied for its deformational and frictional properties in a similar double-direct shear device (Rathbun *et al.*, 2008), allowing direct comparison of measurements. As was done in that study, samples were air-dried and then disaggregated by hand before sieving for grain-size analysis and homogenization. We also removed all grains of greater than 1 mm diameter, following the soil mechanics recommendation of having no grains larger than 1/10th the layer thickness (Head, 1989). This ensured that the layer was homogenous, and no large particles dominated the mechanical response. Till characterization and comparison to friction measurements in Rathbun *et al.* (2008) are included in Appendix A.

The side blocks have a steel plate on the till-facing surface, with 0.8 mm deep and 1 mm spaced grooves, to insure there is no sliding on the till–block interface, so that all imposed displacement is on the ice–till interface or within the till layer. We also machined a grooved central steel block to measure till-only deformation under equivalent conditions and, thus, by comparison to the more complex system, isolate the effect of the added ice–till interface. In a frozen till-only configuration, the central block groves did not fully couple to the frozen till. Because the measurement of friction between the frozen till and steel is not useful for understanding frozen till deformation, these data are not provided. Because all measurements were done under nominally wet or frozen conditions, the till was loaded wet, as it is more cohesive and easier to work with that way. In all cases, the till layers were prepared by packing the till onto the grooved steel plate surface of the side blocks surrounded by a cellophane tape wall and measured to a height of 10 ± 0.5 mm using a leveling jig. Experiments with till thickness of 5 mm showed equivalent frictional behavior (see the Supplement Section S2), so all reported experiments are with 10 mm layers. Till samples were preloaded by dead weight to 22 kPa for about 5 min in the leveling jig, which pushed out any excess pore water.

Using standard practices for double-direct shear of granular gouges (Rathbun *et al.*, 2008), clear plastic side shields were attached to the unstressed front and back, whereas, thin copper shims were attached to the top and bottom of each side block to retain the nominal shape and surface area of the till during initial normal stress loading. The three blocks (central ice or grooved steel and two side blocks with till layers) are stacked vertically to cover top till surfaces, from here on referred to as the sample assembly. A thin parafilm sheet was stretched across the bottom of the sample assembly, to avoid loss of till grains during deformation, but, pore and melt water is able to drain freely at atmospheric pressure, as visually observed. The resistance from the parafilm was measured with the vertical load cell, to contribute less than 1 kPa to the measured shear stress, and is independent of driving velocity and displacement (not elastic).

Cryogenic biaxial apparatus

Experiments were conducted using an ambient pressure, cryogenic temperature, servo-hydraulic biaxial friction apparatus (McCarthy *et al.*, 2016). Modification to the insulating cryostat and loading procedure was required to load the entire three-block assembly into the apparatus and precisely control temperature. The new cryostat (Fig. 1) included plumbing for circulating chiller fluid into the side blocks and resistance temperature detector (RTD) ports directly below the grooved steel plate and till layer, allowing direct temperature monitoring and control, as well as Peltier thermoelectric coolers directly in front of and behind the ice block to limit melt. Ultra Precise RTD sensors (Manufacturer: Omega) record temperature every second, with an accuracy of ±0.15°C. The temperature was measured and controlled directly behind the till, so reported temperatures are for this location. For temperatures above freezing, the ice should be at its pressure melting point, whereas, the ice should be close to the control temperature when below freezing. The entire cryostat was made of insulating material, including a fiberglass base, to minimize heat transfer. A transparent Plexiglas front panel allowed for monitoring of the interface during the experiment. Cooling was controlled both by fluid temperature and by manual control of fluid flow rate to within <0.25°C difference between the two sides. Oscillations in chiller duty cycle contributed to a total variance of <0.3°C throughout the hour-long experiment. Because of these oscillations, we chose to control the till at temperatures sufficiently far from the melting point, to avoid uncontrolled melting and refreezing throughout the experiment run time. Figures 2a show the temperature stability of a representative run.

The horizontal piston applied normal stress by motion of a thermally insulating Macor rod acting against another fixed rod on the other side. Load cells located outside the cryostat measured load on either side. Because of plumbing and RTDs slightly restricting side block motion, stress changes did not transfer completely between the two horizontal load cells, with differences in normal stresses up to ~30%. Thus, reported normal stresses and friction were calculated from the average between the two load cell measurements. Measured stresses are always averaged values over the surface area, so averaging the two interfaces normal stresses best captures the entire sample. Because variations in this difference between the two normal stresses between experiments (most extreme cases for each sample type are plotted in Figs. S4, S5, and S6) do not appear to change the frictional behavior, and broader frictional behavior calculated using either load cell is equivalent (Fig. S7), we do not believe it represents a significant experimental artifact. The difference between normal stresses changed with experimental velocity, so is interpreted to be due to the state of the till layer, thus providing additional information on the till's dilation and compaction (discussed further in the Supplement Section S3). We found that the load cells were more sensitive to these processes than was the measured horizontal displacement, which had a steady inward movement to maintain constant stress while sample thickness decreased due to ice melt. This measured displacement was used to estimate melt rate (~0.25 μm/s at ~0.5°C).

The vertical piston pushed the central ice sample down through the till layers at a programmed load-point velocity. A direct current differential transformer provided the displacement feedback. A load cell mounted to the vertical Macor rod on the outside of the cryostat provided the shear stress measurement. The vertical load is balanced over both till surface cross-sectional areas on either side of the ice block ($2 \times 50 \times 50$ mm^2) providing the shear stress, whereas, the horizontal load is balanced by each cross-section area independently (50×50 mm^2), providing the normal stress, the ratio of the two gives the friction (μ), assuming a y-intercept near zero, or negligible cohesion to provide shear strength at zero normal stress. Measuring under a range of normal stresses, we confirm that cohesion is negligible in most cases, addressed in Appendix A.

Experimental procedure

A total of 31 friction experiments are presented with various configurations of till and central block, as provided in Table 1. We tested the frictional dependence on many conditions (including till layer thickness, largest grain size, and normal stress), but this study focuses on the experimental parameters

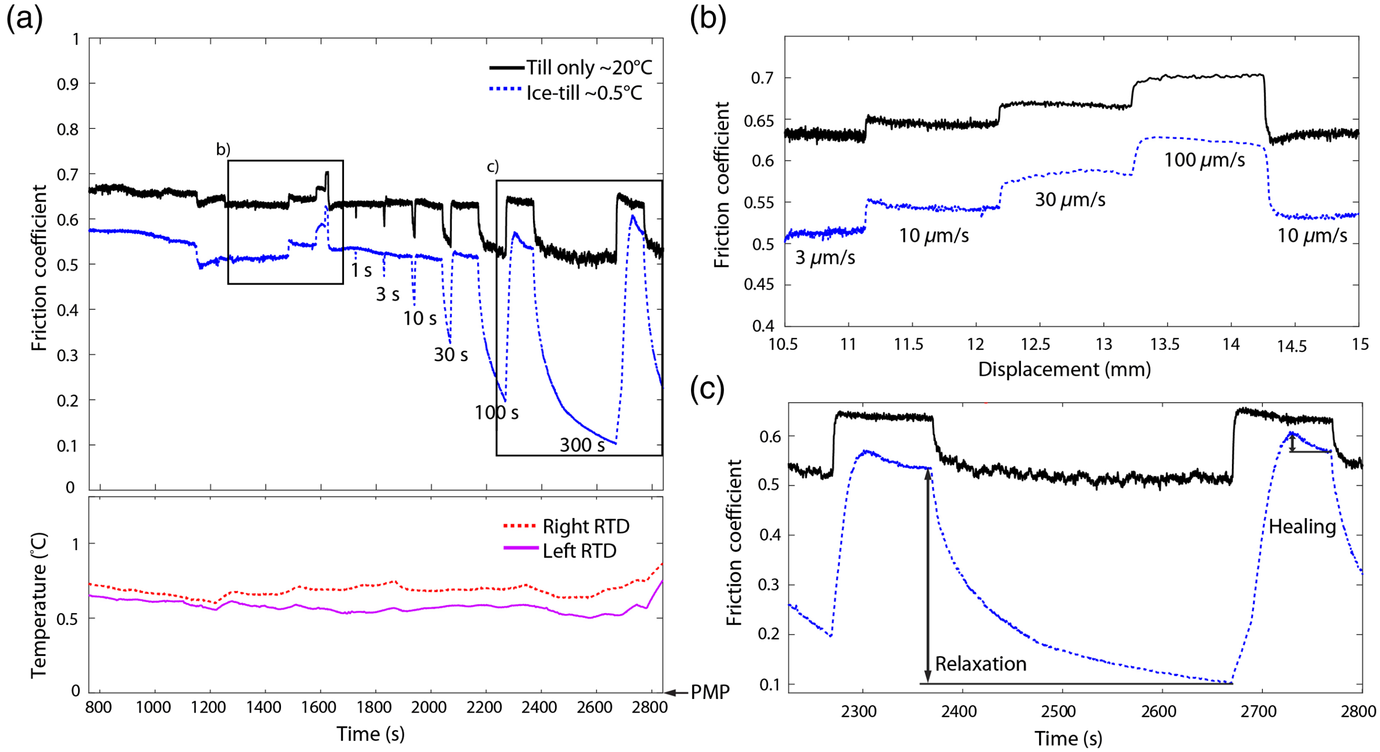

Figure 2. (a) Example experimental runs for sample C0127, pure ice–till (blue dotted line) at ~0.5°C, and C0110, till-only (black) deformation at room temperature (~20°C). The bottom plot shows the temperature from two RTDs (red dotted line is right and magenta solid line is left) behind each till layer during the ice–till (blue) experiment relative to the pressure melting point (PMP). Both experiments follow the same driving velocities and hold times as labeled below the ice–till friction. (b) A zoom-in of velocity steps are plotted as a function of displacement with velocities labeled, whereas, (c) a zoom-in of the 300 s hold is labeled to show how healing and relaxation are measured. The color version of this figure is available only in the electronic edition.

that had the most significant effect on friction (load-point velocity, ice sample debris content, and temperature), other conditional dependencies are presented in supplemental material.

The side blocks with wet till were prechilled in a freezer at ~ -12°C for, at least, 10 min, to help stabilize temperature before loading with ice into the cryostat. The temperature of the side blocks was monitored and controlled, as it reached the selected stabilized temperature. Prechilling minimized ice melt during loading. Once the sample assembly was loaded into the prechilled cryostat, and temperature stabilized, shear was initiated. The employed driving protocol consisted of a long ramp at 10 μm/s for 1000 s (10 mm of displacement), to allow for elastic loading to a peak friction (particularly apparent if the till is overconsolidated, see Fig. S4) and transition to steady-state or critical-state friction. The load point was then driven for a series of velocity steps at 3, 10, 30, and 100 μm/s, each for 1 mm of displacement, then back down to 10 μm/s for a series of slide-hold-slides of 1, 3, 10, 30, 100, and 300 s, for a total displacement of 20 mm. Experiments (C0134 and C0156) with longer velocity steps of 2 mm and no slide-hold-slides were undertaken for longer D_c found at frozen conditions. Example experimental runs for temperate ice–till and till-only configurations are shown in Figure 2.

Each velocity step was fit to the rate-and-state friction law, with a single state variable, (equations 1–3) using the MATLAB (see Data and Resources) graphical user interface RSFit3000 to invert for best-fit parameters (Skarbek and Savage, 2019). Representative example fits for a velocity step is shown in Figure 3. We fit both the aging (equation 2) and slip (equation 3) laws to most examples, with similar fitting parameters, but there are some cases that we were not able to find a slip law fit, so we report parameters for the aging law. For this study, we are only interested in the general range of fitting parameters, so this choice makes little difference to our findings.

We find a range of rate-and-state friction parameters for experiments with nominally equivalent conditions (those listed in Table 1—sample type, temperature, normal effective stress, till layer thickness, largest grain size, and sand content). There are experimental errors associated with each of these, so, to better constrain the range of potential parameters, we average repeated measurements. The 13 equivalent experiments of pure ice–till at melting conditions are underlined in Table 1, average and standard deviation of parameter values are presented in Table 2, and example fits are provided in the

TABLE 1

Experimental Parameters for All Runs, Those Presented in Figures Have the Figure Numbers Listed below the Sample Numbers, Whereas, the 13 Experiments Averaged for Table 2 Are Underlined

Sample Numbers (Figure Numbers)	Ice Type or Till-Only	Temperature (°C)	Normal Load (kPa)	Till Layer Thickness (mm)	Largest Till Grain Size (mm)	Sand Content (% by Mass)
C0091 (S2, S3)	Till only	~20	100	5	0.6	36
C0094 (S1–S3, S8)	Till only	~20	100	10	0.6	36
C0095 (4b, S1–S3)	Bulk pure ice–till	~0.5	100	10	0.6	36
C0096 (4b, S2, S3)	Bulk pure ice–till	~0.5	100	5	0.6	36
C0097 (4b, S1–S3)	Bulk pure ice–till	~0.5	100	10	0.84	40
C0098 (4b, S1–S3)	Bulk pure ice–till	~0.5	100	10	0.84	40
C0099 (7b,d, S5)	Bulk pure ice–till	~ – 3	100	10	0.84	40
C0100 (S1–S3, S8, S9)	Till only	~0.5	100	10	0.84	40
C0103 (S1–S3, S8)	Till only	~20	100	10	0.84	50
C0104 (4b, S1–S3)	Bulk pure ice–till	~0.5	100	10	0.84	50
C0105 (2, S1–S3, S8)	Till only	~20	100	10	0.84	20
C0106 (4b, S1–S3)	Bulk pure ice–till	~0.5	100	10	0.84	20
C0107 (4b, S1–S3)	Bulk pure ice–till	~0.8	100	10	1	100
C0108 (4a, 6, S1–S3, S8)	Till only	~20	100	10	1	100
C0109 (4b, S1–S3)	Bulk pure ice–till	~0.5	100	10	0.064	0
C0110 (2, A1–A2, S2, S8)	Till-only	~20	100	10	0.064	0
C0111 (A1–A2, S1–S3)	Bulk pure ice–till	~0.5	150	10	1	43.2
C0112 (A1–A2, S1–S3, S8)	Till-only	~20	150	10	1	43.2
C0113 (5b, A1–A2, S1–S3, S8)	Till-only	~20	50	10	1	43.2
C0114 (4b, A1–A2, S1–S3)	Bulk pure ice–till	~0.5	100	10	1	43.2
C0118 (4b, S1–S3, S4)	Bulk pure ice–till	~0.5	100	10	1	43.2
C0123 (4b, B1–B2)	Bulk pure ice–till	~0.5	50	10	1	43.2
C0124 (4b, S1–S3)	Standard pure ice–till	~0.5	100	10	1	43.2
C0125	Debris-laden ice–till	~0.5	100	10	1	43.2
C0127 (2–4, 6)	Standard pure ice–till	~0.5	100	10	1	43.2
C0128 (5, 6)	Debris-laden ice–till	~0.5	100	10	1	43.2
C0134 (6, 7a,b)	Bulk pure ice–till	~ – 3	100	10	1	43.2
C0151 (B2)	Bulk pure ice–till	~ – 3	50–150	10	1	43.2
C0156 (5, 6)	Debris-laden ice–till	~ – 3	100	10	1	43.2
C0157 (B2)	Debris-laden ice–till	~0.5	50–350	10	1	43.2
C0160 (B2)	Debris-laden ice–till	~ – 3	50–350	10	1	43.2

Supplement Section S5. The other types of experiments (debris-laden ice and frozen temperatures) are only interpreted for general behavior, because they were only run two times each. Order of magnitude estimates are provided for calculating rheological critical stiffness, but we do not report a specific range of rate-and-state friction parameters in these cases.

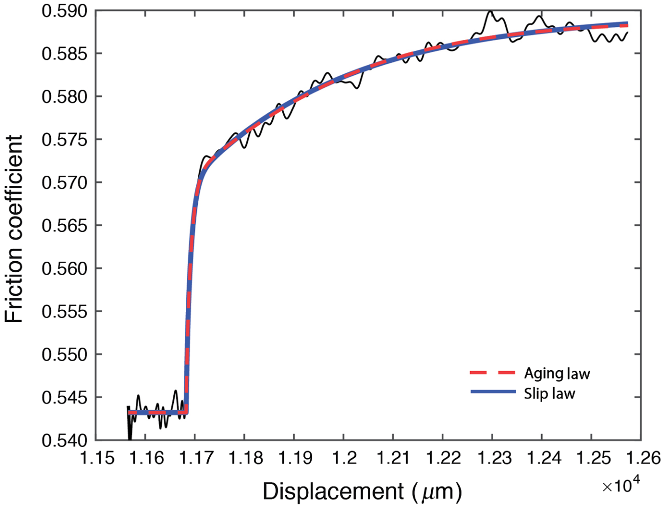

Figure 3. Example velocity step (from 10 to 30 μm/s) from sample C0127 and rate-state friction fits obtained with RSFit3000. This is representative of all melting temperature (~0.5°C) ice–till measurements in which b is very small or negative. Black lines are the data; the red dashed line is the aging law fit; and the blue solid line is the slip law fit. The fits and parameters for the two evolution laws are not significantly different in this and most other cases, but there are examples when we were unable to fit a slip law fit, so we report aging law parameters. The color version of this figure is available only in the electronic edition.

Results

Pure, temperate ice–till steady-state velocity dependence and healing

Figure 4 shows results from a series of ice–till and till-only experiments at temperatures above the pressure melting point (−0.0074°C at 100 kPa using the Clausius–Clapeyron equation). We ran a till-only experiment at this temperature, but, as expected, wet till has little temperature dependence when it is above freezing (see the Supplement Section S4), so reported experiments in this section for till-only deformation were undertaken at room temperature (~20°C). We found a range of friction values for our eight temperate till-only measurements, so the till-only sample with the closest friction value to the highest velocity ice–till friction was selected for ice–till and till-only comparisons, discussed further in the Supplement Section S4. As shown in the literature for many natural tills (Iverson, 2010), we find that the wet Matanuska till has slightly rate-strengthening friction (Fig. 4a). The addition of an ice–till interface gives greater velocity dependence, and larger relaxation and healing (Fig. 2). The steady-state friction at each velocity is determined by taking mean friction for each velocity step, once steady state is reached; the standard deviation, over these same time periods, provide error bars (Figs. 4a, 5b, and 6). Both the healing (Zoet and Iverson, 2018) and steady-state velocity dependence (Zoet and Iverson, 2020) are comparable to those measured by meter-scale ice–till measurements at the pressure melting point; differences in the apparatuses are discussed in Appendix C. We find measurable healing, fitting with a cutoff time (t_c) healing relation for change in friction ($\Delta\mu$) as a function of hold time (t_h)

$$\Delta\mu = \beta \ln\left(\frac{t_h}{t_c} + 1\right), \tag{6}$$

in which β is the healing rate parameter. Our healing shows a lower cutoff time ($t_c \sim 10$ s) and slightly higher healing rate ($\beta \sim 0.021$), than in meter-scale samples at the same driving velocity ($t_c \sim 64$ s and $\beta \sim 0.019$) (Zoet and Iverson, 2018; Fig. 4c). We find no clear trend with velocity for the stability parameter $a - b$ (Fig. 4b). Table 2 provides averages of all parameter values obtained from fitting 53 velocity steps across 13 experiments. These are the first reported rate-and-state friction parameters for ice–till slip in the literature and can, thus, provide useful inputs to rate-and-state models applied to these environments (Minchew and Meyer, 2020). As a reference, fitted a and b parameters are much less than those of a pure ice-on-rock system, whereas, D_c fits here are orders of magnitude larger (C. McCarthy, *et al.*, unpublished manuscript, 2021, see Data and Resources), although, D_c is very poorly constrained when b is small, because very little evolution occurs.

Debris-laden, temperate ice–till steady-state velocity dependence and healing

Figure 5 shows results from experiment (C0128) of debris-laden ice (as described in the Ice Sample Types section) slid against a till layer, at the same temperate conditions (~0.5°C), velocity, and normal stress as the pure ice experiments reported earlier. The results show slightly higher friction values than those of pure ice–till. The measured friction in the debris-laden ice–till system

TABLE 2

Best-Fit Rate-and-State Aging Law Parameters from Fits to Velocity Steps Using RSFit3000

a ± Standard Deviation	**b ± Standard Deviation**	**$a - b$ ± Standard Deviation**	**D_c ± Standard Deviation (μm)**	**k ± Standard Deviation (μm^{-1})**
0.029 ± 0.017	−0.0066 ± 0.023	0.035 ± 0.032	144 ± 139	0.0052 ± 0.0065

Mean and standard deviation of parameters are from 53 steps in 13 samples of pure ice at ~0.5°C. All $a - b$ values are plotted as a function of velocity in Figures 4b and 10; example fits from four experiments are provided in the Supplement Section S5.

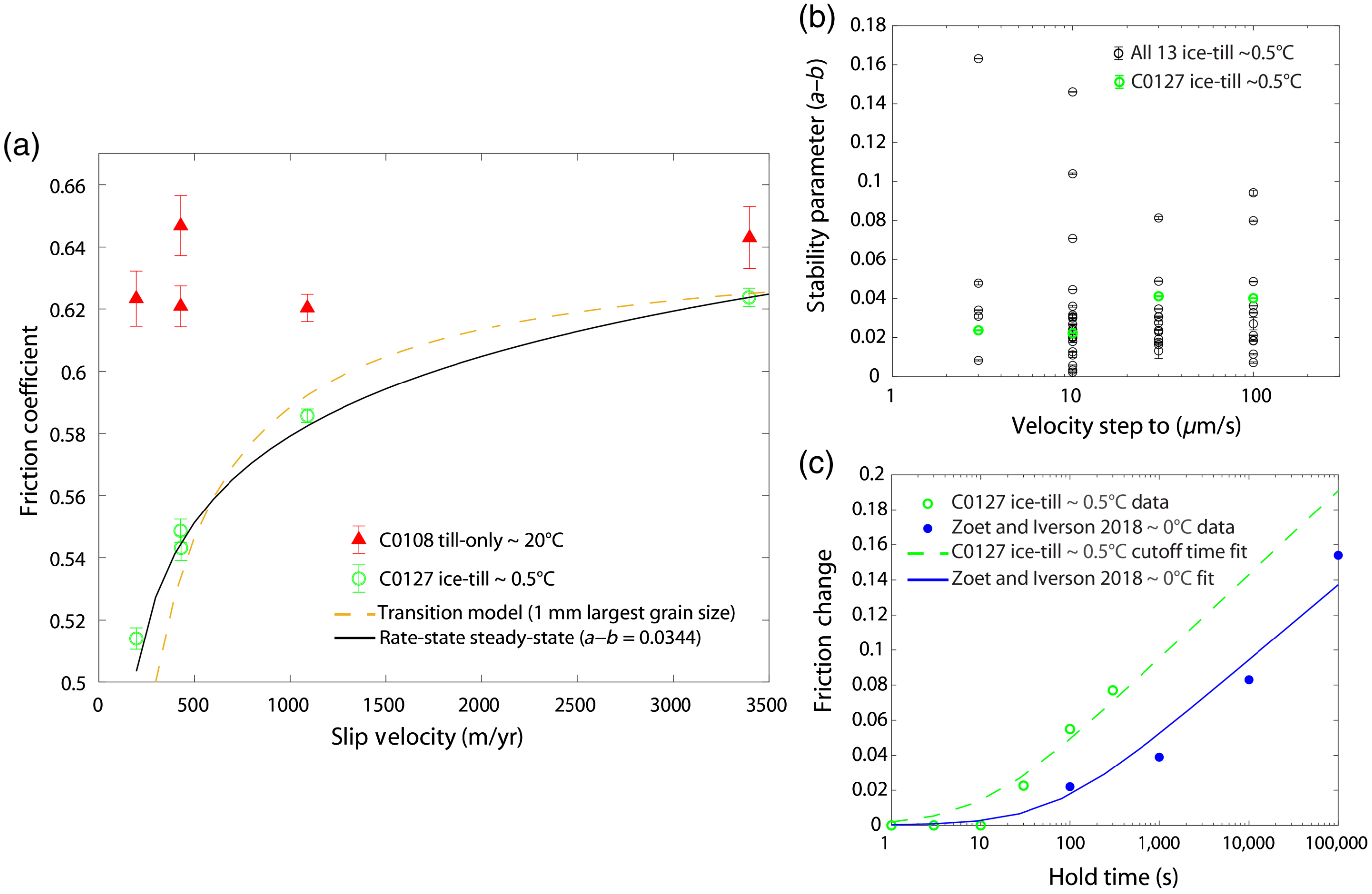

Figure 4. (a) Steady-state friction velocity dependence for sample C0108, till-only (at room temperature ~20°C), in red filled triangles and sample C0127 pure ice–till (at ~0.5°C) in green open circle. Values are the mean during steady state at each velocity, and error bars are the standard deviation during that period. The transition model (equation B2) in orange dotted line (Zoet and Iverson, 2020), calculated using 1 mm the largest till grain size and till-only friction coefficient, and the rate-and-state steady-state friction model (black solid line; equation 4) with $a - b$ calculated from the mean of all fitted steps and holds from this experiment ($a - b = 0.0344$) are also plotted. (b) Rate-and-state friction $a - b$ parameters from 13 experiments of equivalent conditions show no clear velocity dependence for pure ice–till at ~0.5°C. Error bars are from the error best-fit parameter.
(c) Change in peak friction above steady state due to healing as a function of hold time in green open circles, compared with that found in Zoet and Iverson (2018) (blue filled circles). Our data are at ~0.5°C and 100 kPa normal stress, whereas, Zoet and Iverson (2018) is at ~0°C and 150 kPa, both measurements used 10 μm/s slides. Both are fit to cutoff time with equation (6), rate parameters are comparable between the two experiments, but our cutoff time was less (10 s vs. 64 s). The color version of this figure is available only in the electronic edition.

is equivalent to till-only friction at high velocity (>30 μm/s), but is lower at low velocities (<10 μm/s), exhibiting a clear velocity-strengthening behavior (Fig. 5b). The results also show little healing compared with the pure ice case (Fig. 5a vs. Fig. 2c).

Pure and debris-laden ice on frozen till velocity dependence and healing

Lastly, we report a set of pure ice–till and debris-laden ice experiments at temperatures slightly below freezing (−3°C). McCarthy *et al.* (2017) showed that ice on rock friction increased, and the stability parameter decreased with decreasing temperature. We find a more dramatic change in friction at subfreezing temperatures, with friction levels increasing above 1 for both pure ice–till and debris-laden ice–till cases (Fig. 6). Although, the debris-laden ice-on-till friction remains roughly velocity neutral (Fig. 5a,c), we find the first clear velocity-weakening behavior at velocities above 10 μm/s (~330 m/yr) in pure ice–till slip at −3°C. The velocity steps show much longer D_c at these frozen temperatures (Fig. 7a), making it harder to reach steady-state friction. We do not have enough subfreezing experiments for averaging rate-and-state parameters, but the fits from the −3°C steps are well constrained, showing negative $a - b$ values above 10 μm/s that decrease further with increasing velocity (Fig. 7c). Zoet *et al.* (2013) found similar velocity dependence, but less change with velocity, for debris-laden ice on rock at −3°C. These conditions also exhibit healing at longer hold times (Fig. 7b), with friction change increasing linearly with time (Fig. 7d), thus, unable to be fit with a cutoff time relation (equation 6).

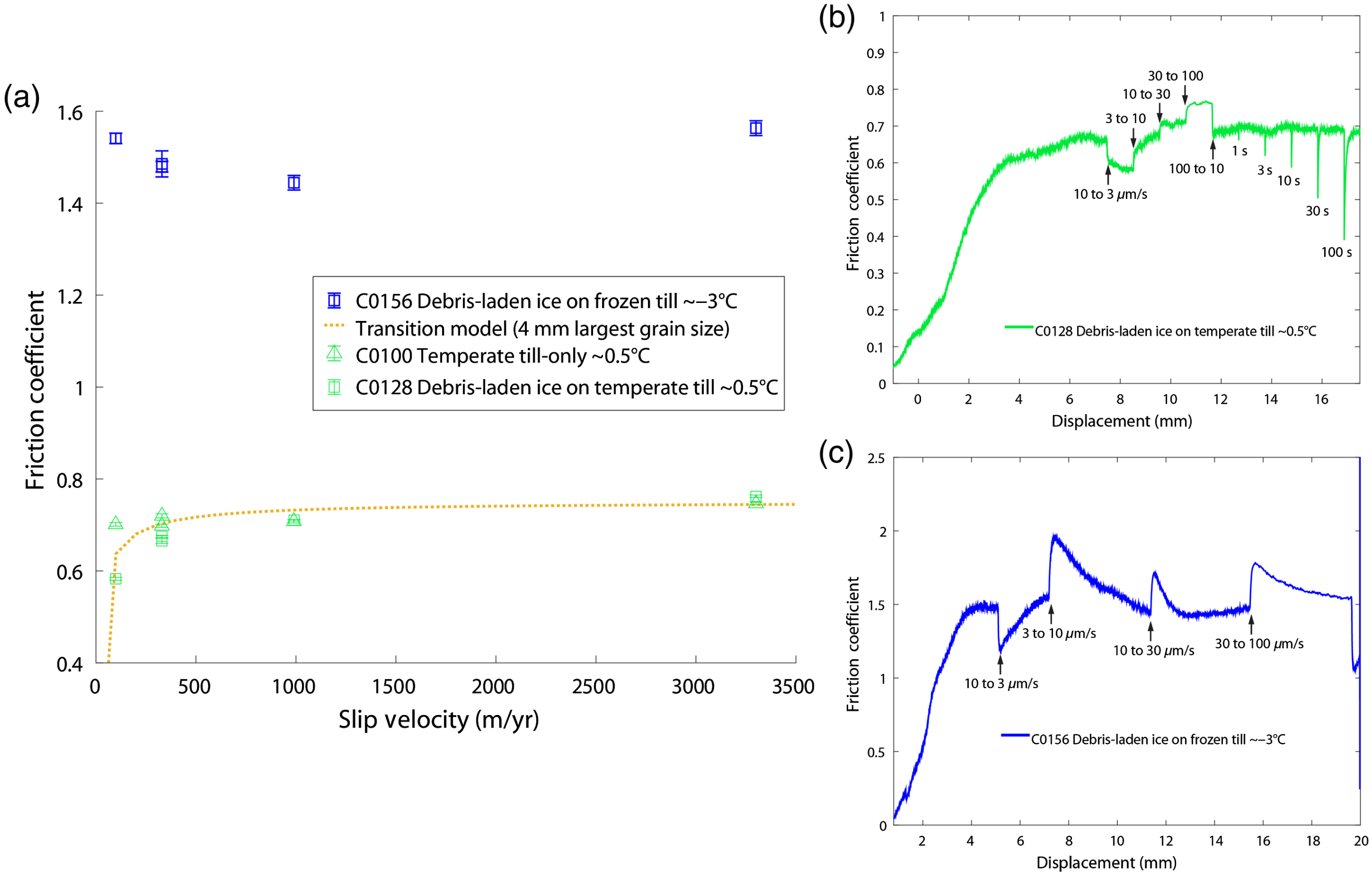

Figure 5. Debris-laden ice on frozen (C0156) and temperate (C0128) till experiments. (a) Steady-state velocity dependence of debris-laden ice on frozen (blue squares) and temperate (green squares) till in comparison to till-only (C0100) in green triangles. At frozen temperatures, friction is high and relatively velocity neutral, whereas, above freezing high-velocity friction reaches till strength, but still fits the lower steady-state friction at low velocities, as predicted by transition model (equation B2; Zoet and Iverson, 2020) calculated for 4 mm largest grain size, as plotted in orange. (b) Friction evolution (green) of debris-laden ice on temperate till (C0128) with velocity steps and slide-hold-slides labeled, velocity strengthening and lack of healing is clear. (c) Friction evolution (blue) of debris-laden ice on frozen till (C0156) with velocity steps labeled, rate-and-state *b*-value is now positive, whereas, friction maintains relatively velocity neutral. The color version of this figure is available only in the electronic edition.

Discussion

Steady-state velocity-strengthening models for pure ice and debris-laden ice on till at melting

We find that frictional sliding of ice on Matanuska till under melting conditions (both pure and debris-laden) is velocity strengthening. Although, this behavior is specific to the till tested, it has also been shown for pure ice on two other tills—one primarily sand (~65%) (Zoet and Iverson, 2020) and the other ~13% sand (Lipovsky *et al.*, 2019); the tested Matanuska sample has an intermediate sand content (~43%). This range of grain-size distributions suggests that till permeability does not greatly change the overall rate dependence, but some till lithology and textures have measured rate weakening consistent with inferred stress drops at WIS (Iverson, 2010). Further ice–till experiments with relevant till samples are needed to assess when rate weakening is possible.

Figure 4a shows the close fit to the rate-and-state steady-state friction law (equation 4), consistent with the velocity-independent stability parameter (Fig. 4b). We also compare with a relation derived from simple physical models for the flow of ice around surface obstacles at low velocities that transitions to clast plowing causing rate-neutral till deformation at higher velocities (equation B2; orange line in Figs. 4a and 5b) (Zoet and Iverson, 2020). The transition model is a functional fit to these two physical models, in which the transition speed is that in which the two shear stresses are equivalent (more details in Appendix B). The model was derived to explain their steady-state velocity data for meter-scale experiments with and without large clasts, so the agreement of our data supports application of the model to a range of scales and relevance of these centimetre-scale experiments.

The transition model was developed for melting temperatures and will always give velocity-strengthening behavior, so cannot be applied to seismic slip. However, the model is appealing for the lack of fitting factors or need for direct

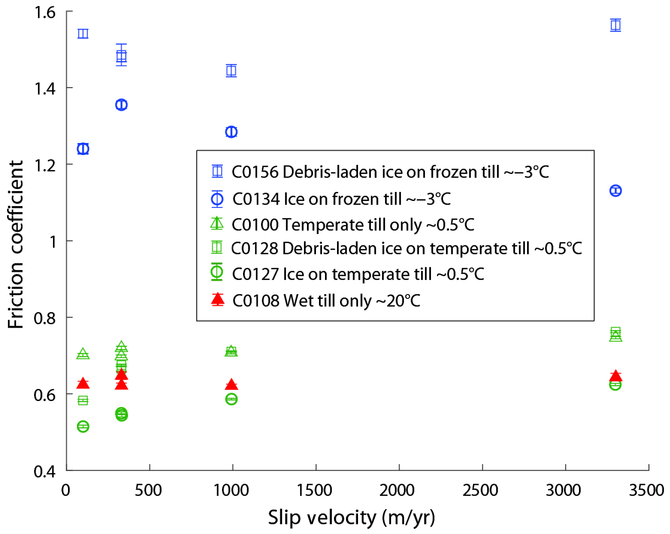

Figure 6. Temperature dependence of steady-state friction in debris-laden ice–till (C0156 at −3°C and C0128 at 0.5°C), pure ice–till (C0134 at −3°C and C0127 at 0.5°C), and till-only (C0100 at 0.5°C, and C0108 at 20°C) experiments. The two temperate till samples (C0100 and C0108) are the highest and the lowest of eight measurements, showing the natural variability in till friction, not temperature dependence (see supplemental material for all till-only data). Colors and fill, as labeled in legend, refer to experimental temperature, while, square are debris-laden ice–till, circles are pure ice–till, and triangles are till-only. The color version of this figure is available only in the electronic edition.

ice–till slip measurements, instead inputs are independently determined experimental parameters (such as effective normal stress) and physical properties of the ice (viscosity, thermal conductivity, latent heat) and till (strength and largest grain size). For the model plots in Figures 4a and 5b, the only parameters that are varied are till strength (from till-only measurements) and largest grain size. Although, grain size follows directly from the sieve size, the till strength is more ambiguous. Our till-only friction coefficient varied by about 0.1 between our eight temperate measurements, so we have to select a sample to match the ice–till measurements; this selection is discussed further in the Supplement Section S4. The agreement between the transition model and rate-and-state steady-state law within this experimental range supports rate-and-state friction's relevance to these settings.

Pure ice heals more than debris-laden ice, linear time dependence at −3°C

Our pure ice–till experiments at melting temperatures show subtle but measurable healing, following a pronounced relaxation (Fig. 2). These results are of similar order to that found at the meter scale (Zoet and Iverson, 2018), as shown in Figure 4c. The lower cutoff time at our high melt rates could help determine the healing mechanism (Nakatani and Scholz, 2004). However, the debris-laden ice experiments show little to no healing, compared with the pure ice experiments at the same temperatures (Figs. 2a and 5a). In contrast, Zoet *et al.* (2013) found healing in debris-laden ice on rock increased with debris content. We also see less healing in till-only deformation compared with the clean ice (Fig. 2), so our till–till and debris–till contacts experience much less healing than ice–till contacts at these conditions, unlike the debris-rock contacts in Zoet *et al.* (2013), potentially due to the compliance of the till substrate relative to rock. Healing is commonly attributed to increasing real contact area during holds due to plastic contact deformation, consistent with our findings, as ice contacts are able to flow and grow more easily than debris contacts. These experiments suggest that debris-laden ice does not increase the likelihood of basal seismicity for a given temperate soft-bed condition, in fact, it might suppress some of the requisite behaviors.

The slide-hold-slide results for pure ice on till at −3°C show significant healing, particularly, at the longest hold time (300 s; Fig. 7d). The healing values below that time are consistent with those of temperate ice–till from this study, as well as those from ice-on-rock at pressure melting conditions (Zoet *et al.*, 2013; McCarthy *et al.*, 2017). However, at 300 s, healing is consistent with ice-on-rock healing at subfreezing temperatures (McCarthy *et al.*, 2017). Functionally, the data can be fit to a linear relationship between friction change and hold time (Fig. 7d). It is not clear at this stage whether the linear fit represents a unique healing mechanism or if sufficiently long hold times are needed to observe the healing rate. If this was the case, longer hold times might show that this linear region conforms to a cutoff time fit of higher β, consistent with ice-on-rock.

Frozen asperities velocity-weakening mechanism

Only for experiments at temperatures below freezing do we observe velocity weakening in pure ice–till slip (Fig. 6). To our knowledge, these experiments report the first measurements of this behavior for ice on till. Both, the pure ice- and debris-laden ice-on-till friction, increases markedly (above values of 1) at freezing temperatures, and cohesion remained negligible (Appendix A). The other main difference we see at subfreezing temperatures is much longer evolution distances to achieve steady state (D_c), such that we needed to increase the length of velocity steps significantly (to 2 mm) to reach steady state (Fig. 7a). The sustained frictional evolution to obtain lower friction at higher velocities suggests a mechanism that requires long displacements.

We appeal to a frictional heating melt lubrication mechanism similar to that proposed by Zoet *et al.* (2013). This is consistent with observations of stability parameter decreasing with increasing velocity (Fig. 7c), as more heating, and, thus, melt, should be generated at higher slip velocities. The friction values at high velocities are still very high (above 1), so there is most

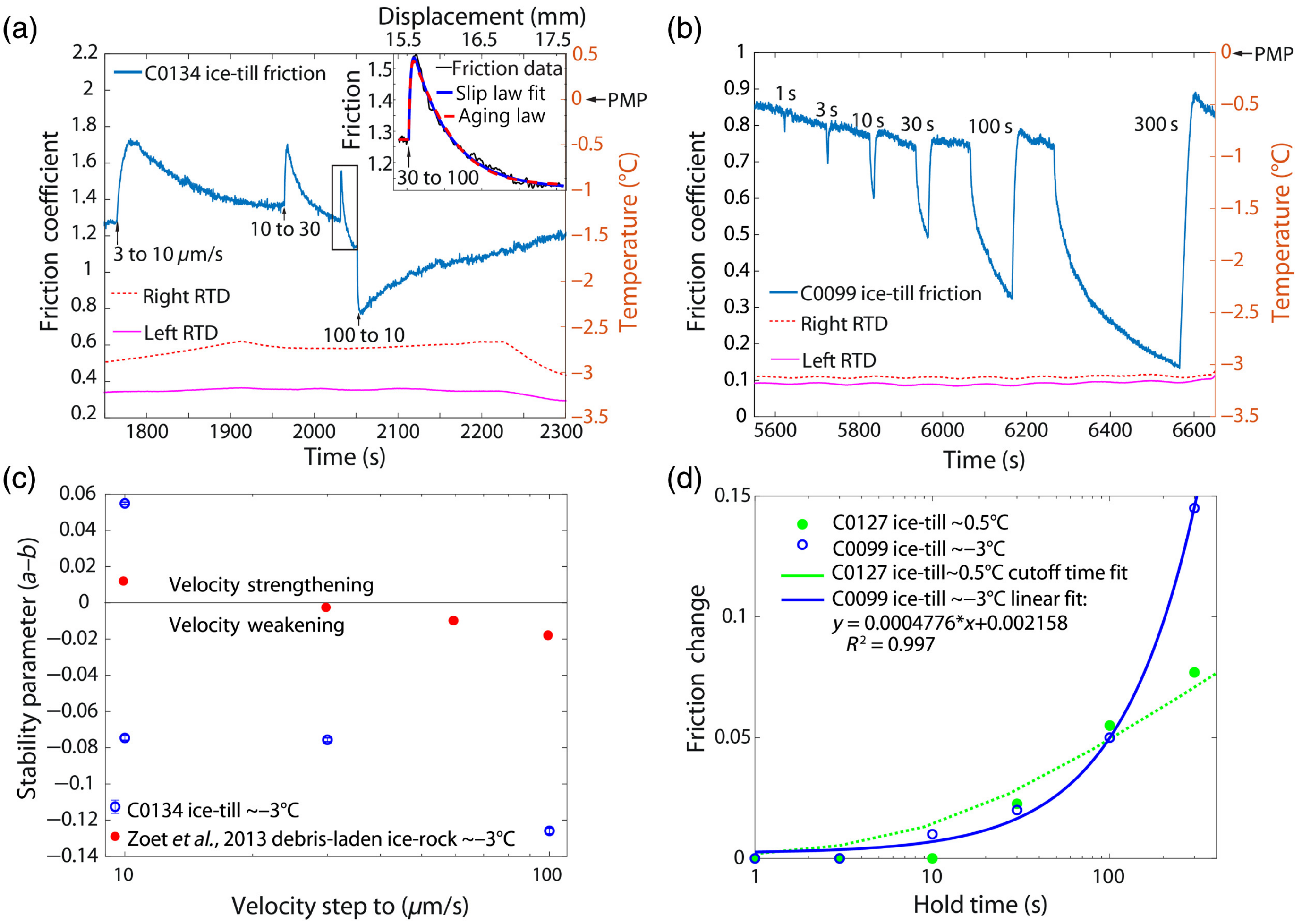

Figure 7. (a) Ice–till at −3°C (C0134) velocity-weakening frictional evolution (blue) for velocities above 10 μm/s, with temperature in each RTD plotted on the right y axis. Experiment had only velocity steps, 2 mm each, to reach steady state due to large D_c. Inset in the upper right shows the rate-and-state friction fits for the 30–100 μm/s step. (b) Ice–till at −3°C (C0099) slide-hold-slides show healing at longer hold times; again, temperature from each RTD is plotted on the right axis. (c) Rate-and-state friction best-fit stability parameter for each step that reaches steady state, as a function of the velocity stepped to, for C0134 (plotted in blue open circles), compared with data from Zoet *et al.* (2013) (red filled circles), natural (16% by weight) debris-laden ice from Engabreen Glacier, Norway on Westerly Granite, also at −3°C but 1.25 MPa of normal stress. The other experiment at −3°C (C0099) did not reach steady state for each step, so the fits and parameters are very poor. Positive $a - b$ at 10 μm/s is a step up from 3 μm/s, whereas, the lower one is a step down from 100 μm/s. Error bars given by the inversion to show the range of parameters that can fit the data. (d) Healing from C0099 (plotted in blue open circles), exhibiting linear dependence on hold time (note logarithmic axis scale), at least in this range of holds, as opposed to the logarithmic dependence that is commonly reported and found at melting temperatures (green closed circles), same data and cutoff time fit as Figure 4c. The color version of this figure is available only in the electronic edition.

likely not a completely lubricated interface, but any melt generated from these higher rates should cause weakening. In contrast to melting temperatures, where any additional melt does not provide significant change in lubrication, cases without free melt (such as frozen) or well-drained (as in dewatered till hypotheses) frictional melt can have a weakening effect with increases in velocity. Because frozen till likely has a very low permeability, any melt generated can build up and significantly lower effective normal stress. Large displacements (D_c) are required to fully realize this weakening and reach a new steady state.

Broad estimations of the frictional heat generation, given the bulk shear stress multiplied by total slip duration, do not provide significant energy to raise a diffusion length thickness of ice to the bulk melting point from −3°C; calculation provided in Appendix D. Yet experiments at lower shear stresses for equivalent slip durations and temperatures have reported evidence of melt (Zoet *et al.*, 2013; McCarthy *et al.*, 2017), suggesting stress concentrations on surface asperities cause higher than bulk shear stresses (increasing the local frictional heating) and normal stresses (decreasing the pressure melting point). In Appendix D, we calculate that stress concentrations on asperities the size of our largest till grains could reach the pressure melting point, if the real area of contact is less than 13.5% of the apparent contact area (relatively large at these low normal stresses), using an asperity flash heating model (Rice, 2006). Other thermal processes, such as premelting (Dash *et al.*, 2006), could contribute to observed weakening as well.

Frozen critical stiffness estimation from rate-and-state friction parameters

The experiments provide estimates for the rate-and-state friction parameters needed to estimate the rheological critical stiffness (k_{cr}), which must be greater than the elastic system stiffness to generate unstable slip (equation 5). This value can be compared with the RSFit3000 inversions of apparatus stiffness to understand what experimental conditions we would need to observe stick-slip cycles. Given the measured $a - b$ of order −0.1 (average of 10–30 and 30–100 μm/s steps shown in Fig. 7c), experimental effective normal stress $\sigma \sim 100$ kPa, and $D_c \sim 500$ μm (again the average of these steps), we use equation (5) to estimate rheological critical stiffness $k_{cr} \sim 0.02$ kPa/μm or 1×10^5 N/m in traditional stiffness units or in friction/μm ~ 0.0002 μm^{-1}. The velocity steps in this experiment gave an average stiffness of ~ 0.01 μm^{-1} (consistent with those found averaging melting temperature experiments given in Table 2), but significantly greater than the estimated rheological critical stiffness, explaining why stick-slip instability was not observed in our experiments. To measure stick-slips at these conditions, we would need to significantly reduce the stiffness of the apparatus. This low value of subcritical stiffness is mostly due to the very large D_c, as $a - b \sim -0.1$ is an order of magnitude lower than that reported in Zoet *et al.* (2013).

The stiffness (k) of subglacial conditions has not been studied in the field, but estimates of seismic patch size (L) and the softer of ice or till shear modulus (G) provide bounds using the following relation:

$$k = \frac{G}{L}. \tag{7}$$

Estimates of these quantities are not independent though, as seismic inversions of slip and patch size require the shear modulus. Because we expect frozen till to be about the same modulus as ice, we use the ice modulus ($G \sim 3$ GPa), but estimates of till shear modulus can be more than 3 orders of magnitude lower (Hudson *et al.*, 2020). This gives a subglacial stiffness ($k \sim 3 \times 10^9$ N/m) more than 4 orders of magnitude larger than our estimated critical stiffness, for small (meter-scale) microseismic asperity patches and still more than an order of magnitude higher ($k \sim 3 \times 10^6$ N/m) for asperities as large as the ice stream thickness (∼1 km). This simple model fails for asperities larger than the ice stream thickness, because the adjacent ice is not able to accommodate the interevent strain, upstream and downstream regions are involved (Winberry *et al.*, 2014). Besides the uncertainty in the relevant shear modulus, effective normal stress in the field is also unknown. Our experiments employed a low effective normal stress ($\sigma \sim 100$ kPa) assumed for ice streams with significant pore-water pressure, so one way to potentially explain this discrepancy is with much higher normal stress due to frozen pore water. This discrepancy between stiffness estimates further highlights the significant constraint on basal conditions that seismicity could provide.

Ice stream setting and glaciological implications

Freeze-on is one mechanism that can cause high shear stress asperities in ice streams (Stokes *et al.*, 2007). Topographic highs and regions of thin ice increase heat loss where "islands" of cold-based ice could freeze till in areas tens of meters to kilometers in horizontal extent (Lliboutry, 1987), consistent with subglacial seismic asperity scales (Aster and Winberry, 2017). Although, the rapid motion of ice streams favors basal melting, if thinning exceeds the supply of ice from upstream, downward advection of cold ice will cause localized freezing basal conditions (Hulbe and MacAyeal, 1999). Evidence for freeze-on has been found in boreholes of active and shutdown ice streams (Kamb, 2001) as well as inferred from paleo-ice stream beds (Stokes and Clark, 2001). Although, frozen conditions are associated more commonly with either shutdown ice streams (Kamb, 2001) or slow-moving parts of ice sheets (Bell *et al.*, 2011) than active fast slip, ice streams are expected to have significant frozen bed area (Joughin, Tulaczyk, *et al.*, 2004). The freeze-on thickness (10–14 m; Carsey *et al.*, 2002) at Kamb Ice Stream (KIS) and contemporary rates (4.2 mm/yr; Kamb, 2001) suggest that freezing conditions likely began before shutdown ∼150 yr ago, presumably contributing to the large-scale flow changes. KIS also currently exhibits significantly more basal seismicity than upstream regions of neighboring, active WIS (Anandakrishnan and Bentley, 1993), supporting the association of seismicity with frozen conditions, although, seismicity observations do not extend to preshutdown times, and the downstream WIS ice plain has extensive seismicity (Winberry *et al.*, 2013). Stick-slip has been suggested to control the ice stream deceleration process (Joughin *et al.*, 2005), so improved understanding of its mechanisms will enhance predictions and seismic monitoring of future ice stream changes.

Overall, because of the importance of lubricating melt water in rapid basal slip, differences in till drainage, porosity, and, thus, stiffness are commonly used to explain ice-stream basal movement, including seismicity. For example, Anandakrishnan and Alley (1997) prefer a dewatering mechanism, whereby, shear localizes as till porosity decreases, for shutdown and seismicity in KIS, but they cannot rule out a contribution from freezing. Because our frozen measurements are only slightly below the pressure melting point, its dry nature is key for achieving velocity weakening. However, our experiments suggest that higher initial friction from freezing might be important for consistent seismic behavior.

We propose that regions of freezing conditions could produce subglacial seismicity as well as high shear stresses. This is a testable hypothesis, because relatively large areas that exhibit seismicity on the ice sheet bed can be investigated through field campaigns to study both their seismicity, and the englacial temperature and strain rate structure. The englacial temperature structure would indicate whether the bed is frozen. Our experiments show that frozen bed conditions represent a dramatic increase in basal shear stress, roughly doubling the friction from temperate conditions. These asperities can then be compared with seismic estimates, where available, and tested for thermodynamic plausibility of freezing with ice stream flow models. Another exercise to test this hypothesis would be to explore how frozen bed regions evolve under different slip and hydrological conditions in ice stream beds. Findings could be compared with basal seismic observations, which vary in their temporal evolution, either repeating in the same location, migrating, or disappearing (Kufner *et al.*, 2020).

Conclusions

We present the first experimental confirmation of velocity-weakening friction in ice–till slip, achieved at frozen temperature (−3°C). In contrast, we find that pure ice–till and debris-laden ice–till slip at melting temperatures are velocity strengthening, in agreement with recent measurements of pressure melting point ice–till slip (Lipovsky *et al.*, 2019), with and without clasts, and consistent with mechanistic models (Zoet and Iverson, 2020). Although, debris-laden ice has been proposed to be a key component of seismicity in soft-bed environments (Lipovsky *et al.*, 2019), we do not find support for this, and the lack of observed healing suggests high debris-content might inhibit stick-slip cycles in till-based glaciers. Because large displacements and high velocities are needed to evolve to the weakened steady-state friction, we suggest that built-up frictional melt is the cause of rate weakening in frozen, low permeability till. Frozen experiments also show strong healing. Multiple mechanisms are likely responsible for the wide-ranging scales of subglacial seismic observations, and laboratory experiments are needed to assess each hypothesis, fully exploiting the constraints provided on seismic bed conditions. To date, experiments have shown velocity weakening in ice-bed friction for debris-laden ice-on-impermeable rock at subfreezing temperature and permeable rock at the pressure melting point (Zoet *et al.*, 2013), pure ice-on-impermeable rock at subfreezing temperature (McCarthy *et al.*, 2017), and, now, pure ice-on-till at subfreezing temperature. Clast plowing has also been shown to cause velocity weakening in till, but without viscous ice, which could potentially mask the pore-pressure feedback, whereas, temperate, pure and debris-laden ice-on-till, and impermeable rock consistently show velocity-strengthening. These findings suggest that some seismic ice stream asperities may express frozen conditions.

Data and Resources

The datasets generated for this study will be found online at doi: 10.6084/m9.figshare.14192669. Supplemental material is uploaded as a separate file, including discussion, figures, and captions. www.mathworks.com/products/matlab (last accessed December 2020). The unpublished manuscript by C. McCarthy, R. M. Skarbek, and H. M. Savage (2021). Effect of periodic sliding velocity on ice friction, *Frontiers in Earth Science: Ice Sheet Shear Margins in Warming Climate: Process and Trends.*

Declaration of Competing Interests

The authors acknowledge that there are no conflicts of interest recorded.

Acknowledgments

S. Saltiel acknowledges the support of the Lamont-Doherty Postdoctoral Fellowship in Earth and Environmental Sciences. Lamont-Doherty Contribution Number 8482. This research and C. McCarthy and H. M. Savage were funded by National Science Foundation (NSF)-1854629. T. Creyts was funded through NSF-1643970. Many thanks to M. A. Nielson, T. Koczynski, and J. Tielke for laboratory assistance, C. Marone and A. P. Rathbun for sharing their Matanuska till friction data, and the Penn State Rock and Sediment Mechanics Lab for experimental advice, as well as N. R. Iverson, B. M. Minchew, C. R. Meyer, and T. Mittal for fruitful discussions. Comments from L. Zoet and an anonymous reviewer also improved the clarity of this article.

References

Anandakrishnan, S., and R. B. Alley (1997). Stagnation of ice stream C, West Antarctica by water piracy, *Geophys. Res. Lett.* **24,** no. 3, 265–268, doi: 10.1029/96GL04016.

Anandakrishnan, S., and C. R. Bentley (1993). Micro-earthquakes beneath ice streams B and C, West Antarctica: Observations and implications, *J. Glaciol.* **39,** no. 133, 455–462.

Aster, R. C., and J. P. Winberry (2017). Glacial seismology, *Rep. Progr. Phys.* **80,** 126801, doi: 10.1088/1361-6633/aa8473.

Barcheck, C. G., S. Y. Schwartz, and S. Tulaczyk (2020). Icequake streaks linked to potential mega-scale glacial lineations beneath an Antarctic ice stream, *Geology* **48,** no. 2, 99–102, doi: 10.1130/G46626.1.

Barcheck, C. G., S. Tulaczyk, S. Y. Schwartz, J. I. Walter, and J. P. Winberry (2018). Implications of basal micro-earthquakes and tremor for ice stream mechanics: Stick-slip basal sliding and till erosion, *Earth Planet. Sci. Lett.* **486,** 54–60, doi: 10.1016/j.epsl.2017.12.046.

Beem, L. H., S. M. Tulaczyk, M. A. King, M. Bougamount, H. A. Fricker, and P. Christoffersen (2014). Variable deceleration of Whillans Ice Stream, West Antarctica, *J. Geophys. Res.* **119,** no. 2, 212–224, doi: 10.1002/2013JF002958.

Bell, R. E., F. Ferraccioli, T. T. Creyts, D. Braaten, H. Corr, I. Das, D. Damaske, N. Frearson, T. Jordan, K. Rose, *et al.* (2011). Widespread persistent thickening of the East Antarctic Ice Sheet by freezing from the base, *Science* **331,** no. 6024, 1592–1595.

Bennett, M. R. (2003). Ice streams as the arteries of an ice sheet: Their mechanics, stability and significance, *Earth Sci. Rev.* **61,** nos. 3/4, 309–339, doi: 10.1016/S0012-8252(02)00130-7.

Bhattacharya, P., A. M. Rubin, and N. M. Beeler (2017). Does fault strengthening in laboratory rock friction experiments really depend primarily upon time and not slip? *J. Geophys. Res.* **122,** no. 8, 6389–6430.

Carsey, F., A. Behar, A. L. Lane, V. Realmuto, and H. Engelhardt (2002). A borehole camera system for imaging the deep interior of ice sheets, *J. Glaciol.* **48,** no. 163, 622–628.

Christoffersen, P., and S. Tulaczyk (2003). Response of subglacial sediments to basal freeze-on 1. Theory and comparison to observations from beneath the West Antarctic ice sheet, *J. Geophys. Res.* **108,** no. B4, doi: 10.1029/2002JB001935.

Clarke, G. K. (2005). Subglacial processes, *Annu. Rev. Earth Planet. Sci.* **33,** 247–276.

Cole, D. M. (1979). Preparation of polycrystalline ice specimens for laboratory experiments, *Cold Reg. Sci. Technol.* **1,** 153–159, doi: 10.1016/0165-232X(79)90007-7.

Cuffey, K. M., and W. S. B. Paterson (2010). *The Physics of Glaciers*, Fourth Ed., Elsevier, New York, New York, 255 pp.

Dash, J. G., A. W. Rempel, and J. S. Wettlaufer (2006). The physics of premelted ice and its geophysical consequences, *Rev. Mod. Phys.* **78,** no. 3, 695.

Dieterich, J. (1979). Modeling of rock friction. 1. Experimental results and constitutive equations, *J. Geophys. Res.* **84,** no. B5, 2161–2168.

Emerson, L. F., and A. W. Rempel (2007). Thresholds in the sliding resistance of simulated basal ice, *Cryosphere Discuss.* **1,** 99–122, doi: 10.5194/tcd-1-99-2007.

Gu, J., J. R. Rice, A. L. Ruina, and S. T. Tse (1984). Slip motion and stability of a single degree of freedom elastic system with rate and state dependent friction, *J. Mech. Phys. Solids* **32,** no. 3, 167–196.

Head, K. H. (1989). *Soil Technician's Handbook*, John Wiley and Sons, New York, New York, 83 pp.

Hudson, T. S., A. M. Brisbourne, F. Walter, D. Gräff, R. S. White, and A. M. Smith (2020). Icequake source mechanisms for studying glacial sliding, *J. Geophys. Res.* **125,** no. 11, e2020JF005627.

Hulbe, C. L., and D. R. MacAyeal (1999). A new numerical model of coupled inland ice sheet, ice stream, and ice shelf flow and its application to the West Antarctic ice sheet, *J. Geophys. Res.* **104,** no. B11, 25,349–25,366.

Iverson, N. R. (1999). Coupling between a glacier and a soft bed: II Model results, *J. Glaciol.* **45,** 41–53, doi: 10.3189/S0022143000003026.

Iverson, N. R. (2010). Shear resistance and continuity of subglacial till: Hydrology rules, *J. Glaciol.* **56,** no. 200, 1104–1114, doi: 10.3189/002214311796406220.

Iverson, N. R., and B. B. Petersen (2011). A new laboratory device for study of subglacial processes: First results on ice–bed separation during sliding, *J. Glaciol.* **57,** no. 206, 1135–1146.

Joughin, I., R. A. Bindschadler, M. A. King, D. Voigt, R. B. Alley, S. Anandakrishnan, H. Horgan, L. Peters, P. Winberry, S. B. Das, *et al.* (2005). Continued deceleration of Whillans Ice Stream, West Antarctica, *Geophys. Res. Lett.* **32,** no. 22, doi: 10.1029/2005GL024319.

Joughin, I., D. R. MacAyeal, and S. Tulaczyk (2004). Basal shear stress of the Ross ice stream from control method inversions, *J. Geophys. Res.* **109,** no. B9, doi: 10.1029/2003JB002960.

Joughin, I., S. Tulaczyk, D. R. MacAyeal, and H. Engelhardt (2004). Melting and freezing beneath the Ross ice streams, Antarctica, *J. Glaciol.* **50,** no. 168, 96–108.

Kamb, B. (2001). Basal zone of the West Antarctic ice streams and its role in lubrication of their rapid motion, in *The West Antarctic ice Sheet: Behavior and Environment*, Vol. 77, 157–199.

Kufner, S. K., A. M. Brisbourne, A. M. Smith, H. S. Hudson, T. Murray, R. Schlegel, J. M. Kendall, S. Anandakrishnan, and I. Lee (2020). Not all icequakes are created equal: Diverse bed deformation mechanisms at Rutford Ice Stream, West Antarctica, inferred from basal seismicity, *Earth Space Sci. Open Arch.* doi: 10.1002/essoar.10504915.1.

Lawson, D. E., J. C. Strasser, E. B. Evenson, R. B. Alley, G. J. Larson, and S. A. Arcone (1998). Glaciohydraulic supercooling: A freeze-on mechanism to create stratified, debris-rich basal ice. I: Field evidence, *J. Glaciol.* **44,** no. 148, 547–562.

Leeman, J. R., D. M. Saffer, M. M. Scuderi, and C. Marone (2016). Laboratory observation of slow earthquakes and the spectrum of tectonic fault slip modes, *Nat. Commun.* **7,** no. 1, 1–6, doi: 10.1038/ncomms11104.

Lipovsky, B. P., C. R. Meyer, L. K. Zoet, C. McCarthy, D. D. Hansen, A. W. Rempel, and F. Gimbert (2019). Glacier sliding, seismicity and sediment entrainment, *Ann. Glaciol.* **60,** no. 79, 182–192.

Lliboutry, L. (1987). Realistic, yet simple bottom boundary conditions for glaciers and ice sheets, *J. Geophys. Res.* **92,** no. B9, 9101–9109.

Marone, C. (1998). Laboratory-derived friction laws and their application to seismic faulting, *Ann. Rev. Earth Planet. Sci.* **26,** no. 1, 643–696.

McBrearty, I. W., L. K. Zoet, and S. Anandakrishnan (2020). Basal seismicity of the Northeast Greenland ice stream, *J. Glaciol.* **66,** no. 257, 430–446.

McCarthy, C., H. M. Savage, T. Koczynski, and M. A. Nielson (2016). An apparatus to measure frictional, anelastic, and viscous behavior in ice at temperate and planetary conditions, *Rev. Sci. Instrum.* **87,** 055112.

McCarthy, C., H. M. Savage, and M. Nettles (2017). Temperature dependence of ice-on-rock friction at realistic glacier conditions, *Phil. Trans. Roy. Soc. Lond. A* **375,** no. 2086, doi: 10.1098/rsta.2015.0348.

Meyer, C. R., A. S. Downey, and A. W. Rempel (2018). Freeze-On limits bed strength beneath sliding glaciers, *Nat. Commun.* **9,** no. 1, 1–6.

Minchew, B. M., and C. R. Meyer (2020). Dilation of subglacial sediment governs incipient surge motion in glaciers with deformable beds, *Proc. Roy. Soc. Lond. A* **476,** no. 2238, doi: 10.1098/rspa.2020.0033.

Moore, P. L. (2014). Deformation of debris-ice mixtures, *Rev. Geophys.* **52,** no. 3, 435–467, doi: 10.1002/2014RG000453.

Nakatani, M., and C. H. Scholz (2004). Frictional healing of quartz gouge under hydrothermal conditions: 1. Experimental evidence for solution transfer healing mechanism, *J. Geophys. Res.* **109,** no. B07201, doi: 10.1029/2001JB001522.

Nye, J. F. (1969). A calculation on the sliding of ice over a wavy surface using a Newtonian viscous approximation, *Proc. Roy. Soc. Lond. A* **311,** 445–467, doi: 10.1098/rspa.1969.0127.

Proctor, A. P., T. M. Mitchell, G. Hirth, D. Goldsby, F. Zorzi, J. Platt, and G. Di Toro (2014). Dynamic weakening of serpentinite gouges and bare surfaces at seismic slip rates, *J. Geophys. Res.* **119,** no. 11, 8107–8131, doi: 10.1002/2014JB011057.

Rathbun, A. P., C. Marone, R. B. Alley, and S. Anandakrishnan (2008). Laboratory study of the frictional rheology of sheared till, *J. Geophys. Res.* **113,** doi: 10.1029/2007JF000815.

Rice, J. R. (2006). Heating and weakening of faults during earthquake slip, *J. Geophys. Res.* **111,** no. B05311, doi: 10.1029/2005JB004006.

Rice, J. R., N. Lapusta, and K. Ranjith (2001). Rate and state dependent friction and the stability of sliding between elastically deformable solids, *J. Mech. Phys. Solids* **49,** no. 9, 1865–1898.

Roeoesli, C., A. Helmstetter, F. Walter, and E. Kissling (2016). Meltwater influences on deep stick-slip icequakes near the base of the Greenland ice sheet, *J. Geophys. Res.* **121,** no. 2, 223–240.

Ruina, A. (1983). Slip instability and state variable friction laws, *J. Geophys. Res.* **88,** 10,359–10,370.

Saltiel, S., P. A. Selvadurai, B. P. Bonner, S. D. Glaser, and J. B. Ajo-Franklin (2017). Experimental development of low-frequency shear modulus and attenuation measurements in mated rock fractures: Shear mechanics due to asperity contact area changes with normal stress, *Geophysics* **82,** no. 2, M19–M36, doi: 10.1190/geo2016-0199.1.

Scholz, C. H. (2002). *The Mechanics of Earthquakes and Faulting*, Cambridge University Press, Cambridge, United Kingdom, 82 pp.

Segall, P., and J. R. Rice (1995). Dilatancy, compaction, and slip instability of a fluid-infiltrated fault, *J. Geophys. Res.* **100,** no. B11, 22,155–22,171, doi: 10.1029/95JB02403.

Sergienko, O. V., T. T. Creyts, and R. C. A. Hindmarsh (2014). Similarity of organized patterns in driving and basal stresses of Antarctic and Greenland ice sheets beneath extensive areas of basal sliding, *Geophys. Res. Lett.* **41,** no. 11, 3925–3932, doi: 10.1002/2014GL059976.

Skarbek, R. M., and H. M. Savage (2019). RSFit3000: A MATLAB GUI-based program for determining rate and state frictional parameters from experimental data, *Geosphere* **15,** no. 5, 1665–1676.

Smith, A.M. (2006). Microearthquakes and subglacial conditions, *Geophys. Res. Lett.* **33,** no. 24, doi: 10.1029/2006GL028207.

Stokes, C. R., and C. D. Clark (2001). Palaeo-Ice streams, *Quaternary Sci. Rev.* **20,** no. 13, 1437–1457.

Stokes, C. R., C. D. Clark, O. B. Lian, and S. Tulaczyk (2007). Ice stream sticky spots: A review of their identification and influence beneath contemporary and palaeo-ice streams, *Earth Sci. Rev.* **81,** nos. 3/4, 217–249.

Thomason, J. F., and N. R. Iverson (2008). A laboratory study of particle ploughing and pore-pressure feedback: A velocity-weakening mechanism for soft glacier beds, *J. Glaciol.* **54,** no. 184, 169–181.

Thompson, A. C., N. R. Iverson, and L. K. Zoet (2020). Controls on subglacial rock friction: Experiments with debris in temperate ice, *J. Geophys. Res.* **125,** no. 10, e2020JF005718.

Thøgersen, K., A. Gilbert, T. V. Schuler, and A. Malthe-Sørenssen (2019). Rate-and-state friction explains glacier surge propagation, *Nat. Commun.* **10,** no. 1, 1–8, doi: 10.1038/s41467-019-10506-4.

Tulaczyk, S., W. B. Kamb, and H. F. Engelhardt (2000). Basal mechanics of Ice Stream B, west Antarctica: 2. Undrained plastic bed model, *J. Geophys. Res.* **105,** no. B1, 483–494, doi: 10.1029/1999JB900328.

Umalauft, J., F. Linder, P. Roux, T. D. Mikesell, M. M. Haney, M. Korn, and F. Walter (2020). Stick-slip tremor beneath an alpine glacier, *Geophys. Res. Lett.* **48,** doi: 10.1029/2020GL090528.

Winberry, J. P., S. Anandakrishnan, R. B. Alley, R. A. Bindschadler, and M. A. King (2009). Basal mechanics of ice streams: Insights from the stick-slip motion of Whillans Ice Stream, West Antarctica, *J. Geophys. Res.* **114,** no. F1, doi: 10.1029/2008JF001035.

Winberry, J. P., S. Anandakrishnan, R. B. Alley, D. A. Wiens, and M. J. Pratt (2014). Tidal pacing, skipped slips and the slowdown of Whillans Ice Stream, Antarctica, *J. Glaciol.* **60,** 795–807.

Winberry, P., S. Anandakrishnan, D. A. Wiens, and R. A. Alley (2013). Nucleation and seismic tremor associated with the glacial earthquakes of Whillans Ice Stream, Antarctica, *Geophys. Res. Lett.* **40,** no. 2, 312–315.

Zoet, L. K., and N. R. Iverson (2018). A healing mechanism for stick-slip of glaciers, *Geology* **46,** no. 9, 807–810.

Zoet, L. K., and N. R. Iverson (2020). A slip law for glaciers on deformable beds, *Science* **368,** no. 6486, 76–78.

Zoet, L. K., S. Anandakrishnan, R. B. Alley, A. A. Nyblade, and D. A. Weins (2012). Motion of an Antarctic glacier by repeated tidally modulated earthquakes, *Nature Geosci.* **5,** no. 9, 623–626, doi: 10.1038/ngeo1555.

Zoet, L. K., B. Carpenter, M. Scuderi, R. B. Alley, S. Anandakrishnan, C. Marone, and M. Jackson (2013). The effects of entrained debris on the basal sliding stability of a glacier, *J. Geophys. Res.* **118,** 656–666.

Zoet, L. K., M. J. Ikari, R. B. Alley, C. Marone, S. Anandakrishnan, B. M. Carpenter, and M. M. Scuderi (2020). Application of constitutive friction laws to glacier seismicity, *Geophys. Res. Lett.* **47,** no. 21, doi: 10.1029/2020GL088964.

Appendix A

Till characterization and comparison to Rathbun *et al.* (2008)

We measured a simplistic grain-size distribution, separating grains above and below 64 μm, as the lower boundary of sand-size grains. After removing the large grains >1 mm, our Matanuska site 3 sample has 43.2% sand fraction by mass, somewhat smaller than the 87.2% and 54.8% found for Matanuska sites 2 and 4, respectively, after the same removal procedure (Rathbun *et al.*, 2008).

We compare our measured friction and cohesion of Matanuska till to measurements of other samples from the same till in Rathbun *et al.* (2008). They measured the till shear strength over normal stresses from 50 kPa to 5 MPa, finding both samples fit a linear relationship with friction angle of 31.4°, or 0.61 friction coefficient and 16.6 kPa of cohesion, despite different grain-size distribution. This cohesion is considered negligible, as has been found for a variety of tills (Iverson, 2010), but cohesion has not been explored for ice on till friction. We measured a relatively small range of low normal stresses (50–150 kPa) for temperate ice–till and till-only deformation, as well as frozen ice–till configurations, confirming negligible cohesion in both the till-only and ice–till temperate cases (Fig. A1). Surprisingly, although, frozen ice–till has significantly higher friction coefficient (from ~0.55 to ~1.27), the cohesion remains negligible (Fig. A2). We also find remarkably similar friction coefficient (0.62) as that reported in Rathbun *et al.* (2008), further supporting the frictional

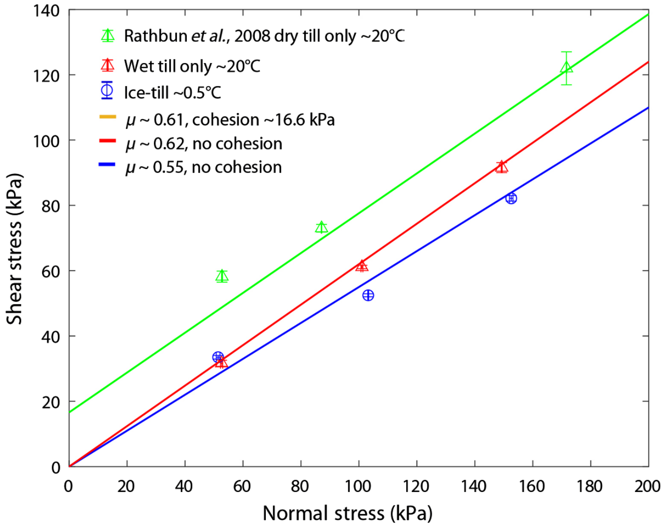

Figure A1. Shear stress as a function of normal stress measured at 10 μm/s load-point velocity. Till-only deformation shown in red triangles gives friction coefficient $\mu = 0.62$, compared with 0.61 reported for till samples from the same glacier (experiment p571 plotted in green triangles) at 1–2 μm/s, with linear fit to data over a wide range of normal stresses (50 kPa to 5 MPa) (Rathbun *et al.*, 2008), and ice–till ($\mu = 0.55$) at 10 μm/s in blue circles. Both fits show near zero *y*-intercept, confirming negligible cohesion, less than found by Rathbun *et al.* (2008) for dry till. Rathbun *et al.* (2008) did not measure Matanuska till saturated, but, measured Caesar till under both dry and saturated conditions, finding that its dry cohesion (29.6 kPa) disappeared (–6.5 kPa) when wet, consistent with our results. Error bars were calculated from standard deviation of shear and normal stress during steady state. The color version of this figure is available only in the electronic edition.

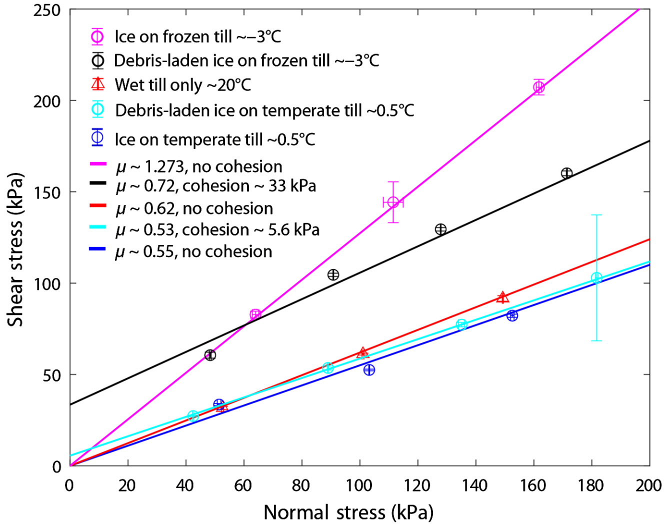

Figure A2. Shear stress, as a function of normal stress, measured at 10 μm/s load-point velocity, including debris-laden and frozen temperature samples. Ice–till at –3°C exhibits much higher shear stresses, giving a friction coefficient more than twice as high, but it still shows negligible cohesion. The debris-laden ice samples have significantly higher surface and thus show some cohesion (~33 and 5.6 kPa for frozen and temperate temperatures, respectively). The debris-laden ice on frozen till is the only sample with any considerable cohesion, but the limited, very low normal stress data points (50 kPa) suggest that the friction coefficient may increase at low normal stress toward the origin, consistent with the change in contact area expected from Hertz contacts on hard surfaces (Thompson *et al.*, 2020). The color version of this figure is available only in the electronic edition.

insensitivity to till grain-size distribution. The ice–till has somewhat lower friction (0.55), as expected. If the ice–till interface is stronger than the till, than till deformation should dominate the resistance. All further reported experiments were controlled at 100 kPa of normal stress, although, the discrepancy between left and right load cells causes some variation in the mean normal stress, as reported.

Appendix B

Transition model of Zoet and Iverson (2020)

Detailed model derivation can be seen in the supplemental materials of Zoet and Iverson (2020), but here we provide the mathematical form of the transition model plotted in Figures 4a and 5b. First, the transition speed (u_t), in which shear stress on a clast from ice flowing around it (Nye, 1969), equals the shear stress resisting that same clast size (R), largest till grain size in cases without clasts, plowing through till (Iverson, 1999):

$$u_t = \left(\frac{\left(\frac{1}{\eta_i (Ra)^2 k_0^3} + \frac{4C_1}{k_0 (Ra)^2} \right)(N_F N)}{(2 + N_F k)} \right), \tag{B1}$$

in which $\eta_i = 3.2 \times 10^{12}$ Pa · s is the ice effective dynamic viscosity, $a = 0.25$ is the fraction of clast radius above the ice–till interface, $k_0 = 2\pi/4R$, $C_1 = C_{pr}K/L$ is the regelation parameter, in which $C_{\mathrm{pr}} = 7.4 \times 10^{-8}$ K/Pa is ice's melting point depression with pressure, $K = 2.55$ w/mK is the mean thermal conductivity of ice and rock, and $L = 3 \times 10^8$ J/m^3 is the volumetric latent heat of ice, $N_F = 33$ is the till-bearing capacity factor estimated from a theory of cone penetration for soils, $N = 100$ kPa the experimental normal stress, and $k = 0.1$ is the pressure-shadow factor. A low value is chosen to represent the regelation dominate behavior expected for clasts under ~0.11 m.

Zoet and Iverson (2020) took the mean of a range of clast sizes to find a functional form with a more gradual transition between the two simplified physical models, providing a slip law:

$$\tau_b = N \tan(\varphi) \left(\frac{u_b}{u_b + u_t} \right)^{1/p}, \text{ or } \mu = \mu_t \left(\frac{u_b}{u_b + u_t} \right)^{1/p}, \tag{B2}$$

in which τ_b is the basal shear stress (τ_b/N is the friction coefficient), φ is the till friction angle such that $\mu_t = \tan(\varphi)$ is the till friction coefficient (assumed rate-insensitive), u_b is the basal slip speed or load-point velocity in our experiments, and $p \sim 5$ is the slip exponent.

Appendix C

Comparison of ice–till experimental apparatuses

Another deformation type that is used to make ice–till slip measurement is ring shear. The chief advantage of ring shear, in general, is that it allows unlimited displacements, whereas, these experiments are limited to ~20 mm of total displacement per experiment. Although, both configurations include wall friction from till confinement, the double-direct shear configuration also needs to confine the till layer in the direction of shear, which needs to be flexible to allow till deformation. Ring shear apparatuses, for example, the Iowa State University Sliding Simulator (Iverson and Petersen, 2011), tend to be meter-scale, so they may better represent natural scales by allowing maximum till grain sizes of 6 mm, as well representative clasts and longer drainage paths (Thompson *et al.*, 2020), as opposed to 1 mm in our centimeter-scale double-direct shear experiments. The larger scale also allows more imbedded measurement sensors, such as distributed sets of thermistors and fluid pressure sensors. The large ice ring is able to keep a stable temperature close to the pressure melting point, but it is difficult to change temperature with its large thermal mass. Larger scale experiments take much longer to evolve to frictional steady state, necessitating experiment durations of days to weeks, and the need for smaller melt rates. Our experiments, however, are each about an hour long. This shorter run time allows us to run a suite of experiments to test the reproducibility of results and dependence on a range of conditions independently. By comparing findings across these laboratory scales, we hope to build more confidence in the results and their applicability to the field scale.

Appendix D

Frictional heating, diffusion length, and temperature rise calculations

We estimate the bulk temperature rise due to frictional slip in our frozen experiments to evaluate the potential for melt generation. We use the 100 μm/s step in Figure 7a as a frozen example in which bulk shear stresses are the lowest ($\mu \sim 1.1$, giving $\tau \sim 110$ kPa for 100 kPa normal stress) and thus minimum frictional heating. Bulk frictional work per unit area (W_f) can be calculated from the bulk shear stress ($\tau \sim 110$ kPa) and slip distance ($d = 2$ mm) over which it is applied:

$$W_f = \tau d. \tag{D1}$$

This gives 220 $\mathrm{J/m^2}$ as the thermal energy generated by friction, which goes into the temperature rise of the ice. The thickness of ice (h) that experiences this heating can be estimated using the diffusion distance that heat reaches during the duration of the step ($t = 20$ s)

$$h = \sqrt{Dt}, \tag{D2}$$

in which $D \sim 10^{-6}\ \mathrm{m^2/s}$ is the thermal diffusivity of ice, giving an ice thickness of 4.5 mm. The temperature rise (ΔT) can then be estimated using heat capacity ($C_p = 2.04$ kJ/kgK) and density ($\rho = 917\ \mathrm{kg/m^3}$) of ice:

$$\Delta T = \frac{W_f}{\rho C_p h} \sim 0.3\ \mathrm{K}. \tag{D3}$$

This suggests that local stress concentrations may be necessary to explain observed weakening that increases with velocity. The bulk shear and normal stresses are measured over the entire nominal area of interfaces, but it is known that all surfaces have much smaller real area of contact. Local stresses are concentrated on these asperities, producing enhanced frictional heating (W_f) and pressure, which would decrease the melting point.

We estimate the temperature change (ΔT) on real contacts (asperities) with stress concentrations, using an asperity flash heating model (Proctor *et al.*, 2014)

$$\Delta T = \frac{\tau_c}{\rho C_p}\sqrt{\frac{vd}{\pi D}}, \tag{D4}$$

in which τ_c is the contact shear stress (the bulk shear stress τ times the apparent contact area over real contact area A/A_r), $v = 100 \mu\mathrm{m/s}$ is the slip velocity, and d is the contact diameter. We use the largest grain size (1 mm) as an estimate of asperity diameter (d). We do not have a measure of the real area of contact, so we use this relation, along with ice's melting point depression with pressure $C_{\mathrm{pr}} = 7.4 \times 10^{-5}$ K/kPa, to estimate the fractional real area of contact needed for temperature rise to reach melting from the experimental temperature ~3°C, $\Delta T \sim 3K - \sigma(A/A_r)C_{\mathrm{pr}}$. Solving for inverse fractional real area of contact (A/A_r)

$$A/A_r = \frac{3K}{\sigma C_{\mathrm{pr}} + \frac{\tau}{\rho C_p}\sqrt{\frac{vd}{\pi D}}} = 73.9, \tag{D5}$$

or 13.5% fractional real area of contact (A_r/A). Under these stress concentrations, the melting point would lower ~0.55 K, and frictional heating would raise the ice temperature the rest of the ~2.45 K to reach melting. So, melting should occur on local asperity contacts, given a real area of contact less than 13.5% of the apparent area of contact, which is likely, given the low experimental normal stress. For reference, mated tensile rock fractures were measured to not reach that level of fractional real contact area until normal stresses of ~3 MPa or higher (Saltiel *et al.*, 2017).

Manuscript received 28 December 2020
Published online 14 April 2021